27/10/10

Parameters determining the radial propagation of type-I ELMs in ASDEX Upgrade

A. Kirk, H.W. Muller[a], A. Herrmann[a], M. Kocan[a], V. Rohde[a], P. Tamain[b] and the ASDEX Upgrade Team

EURATOM/CCFE Fusion Association, Culham Science Centre, Abingdon, Oxon OX14 3DB, UK
[a]Max-Planck Institut für Plasmaphysik, EURATOM Association, Garching, Germany
[b]Association Euratom-CEA, CEA/DSM/IRFM, CEA-Cadarache, F-13108 St Paul-lez-Durance Cedex, France

Abstract

The radial propagation of type-I ELMs in ASDEX Upgrade has been measured using a number of techniques. The most reliable technique uses a filament probe to measure the time difference between two separated probes and yields a mean radial velocity obtained of ~1.5 kms^{-1}. The radial velocity calculated using a time of flight technique suffers from uncertainties in the start time and yields radial velocities which are 3-4 times lower than those based on the filament probe. The filament probe data shows that the filaments leave the LCFS over a period of up to 400 μs. The $\vec{E} \times \vec{B}$ velocity derived from the floating potential at two poloidally separated probes suffers from the neglect of temperature differences, local turbulence effects and the smoothing used. The mean radial velocity calculated is ~ 1100 ms^{-1} for a smoothing of 0.5 μs (the data acquisition time) decreasing to ~ 850 ms^{-1} for a 5μs smoothing. In spite of the differences in the size of the radial velocity all the methods suggest that V_r is independent on distance from the LCFS for $20<\Delta R_{LCFS}<100$ mm and on ELM size. The ion saturation current e-folding length scales with q_{95} and inversely with the square root of the temperature pedestal. Once these dependencies are accounted for the evolution of the e-folding length with $\Delta W_{ELM}/W_{ped}$ is consistent with V_r being independent of ELM size.

1. Introduction

The energy released from the core plasma during Type I Edge Localised Modes (ELMs) is a key area of study for ITER [1], where the resultant power loadings, both inside and outside the divertor region, have an important impact on the choice of plasma facing materials. Although it is clear that filament structures exist during ELMs (see [2] and reference therein) it is still uncertain what parameters determine how much energy these filaments transport to the wall and how they propagate. In order to determine the impact of the filaments on the first wall, information on the parameters affecting the filament propagation is required. A summary of the measurements of the toroidal/poloidal velocities from all devices, where data are available, is given in reference [3]. All the measurements agree that the filaments initially rotate in the co-current direction with velocities near to the pedestal values, which then decrease with time and distance into the scrape off layer (SOL). Where there is more disagreement is in the radial propagation.

The radial propagation of the filaments has been determined by a number of techniques, which have indicated a large spread in the measured radial velocities (V_r) and all possibilities for the dependence of the radial velocity of the filament as a function of distance from the LCFS i.e. constant, deceleration and acceleration [3]. Some of these differences arise because of the different techniques used to measure the velocities while others are most likely due to the assumptions made.

In view of these uncertainties, a conservative approach has been used to provide an upper estimate for the parallel fluxes to be expected during ELMs at the first wall in ITER

[4]. In that paper it was assumed that the radial propagation velocity does not scale with device size but that V_r scales as $\sqrt{\Delta W_{ELM}}$ (where ΔW_{ELM} is the energy lost from the core plasma due to the ELM) with a maximum value of V_r =1 kms^{-1} for the largest uncontrolled ELM. Divertor lifetime requirements mean that the ELM size must be reduced by a factor of ~20 [4]. These controlled ELMs are assumed to have a radial velocity of ~ 0.2 kms^{-1} and would lead to a relatively small additional power flux to the outer wall and should not cause any significant material erosion. However, if the understanding of at least some aspects of the radial propagation can be improved, it would mean that models could be further constrained and a reduction in the uncertainty of the predictions for ITER obtained.

ASDEX Upgrade is equipped with a variety of diagnostics that can be used to determine the radial propagation of ELM filaments and in this paper the filament radial velocity of the filament as a function of ELM size is determined using several techniques and the results are compared and contrasted. The plasmas studied come from 28 analysed type I ELMy H-mode discharges in a Lower Single Null Divertor (SND) configuration with the ion ∇B drift direction towards the lower targets. The discharges have a range of parameters with plasma current ~0.6-1.0 MA, toroidal field (B_T) ~ 2.0-3.0 T, q_{95} ~3.3-6.6, line average densities ($\bar{n}_e$) ~3.0-10.0x10^{19} m^{-3}, neutral beam heating powers 2.5-10 MW, with stored energy (W_{MHD}) ~0.3-0.7 MJ, pedestal energy (W_{ped}) ~ 60-250 kJ, and a range of ELM energy loss (ΔW_{ELM}) ~2-50 kJ.

The layout of this paper is as follows: in section 2 the velocity will be determined using two radially separated probes. In section 3 the radial propagation velocity will be calculated using measurements of the floating potential to determine the poloidal electrical

field. In section 4 the relationship between the radial velocity and the radial fall off length in the ion saturation current will be addressed and in section 5 the implications of these measurements will be discussed.

2. Determining the radial velocity from two radially separated probes

In order to study filament propagation, a filament probe was specially designed and installed in ASDEX Upgrade [5]. This probe is located at the low field side at about 30 cm above the magnetic axis and can be moved radially by a magnetic drive from a position behind the limiters to 1cm in front of the limiter. The probe consists of nine Langmuir pins: five at different poloidal locations but the same radial location and four at different radial locations. A full description of the probe including the location of the pins is given in reference [5]. The pins used in this analysis are pins 1, 6, 7 and 8 (Figure 1). Pins 1 and 6 are at the same radial location, with pin 7 (8) 3.5 (7) mm radially further away from the plasma. The poloidal separation of the pins depends on the local field line angle: a typical angle of 8.6◦, results in a poloidal separation of 4mm for pins 1 and 6 while pins 6 and 7 (7 and 8) are separated by ~2 mm (see Figure 1). The exact separation depends on the local field and is calculated for each shot used in the analysis.

The first results from this probe were presented in reference [5], which determined the radial propagation of the filaments in a set of discharges that had the same plasma parameters and ELM size. In this current analysis, new results from a wide range of different discharges (described in the previous section) are presented and compared to the measurements of the $\vec{E} \times \vec{B}$ velocity measured in the same shots using the method described in the next section.

Figure 2 shows the target D_α and ion saturation current (I_{SAT}) time traces from pins 1, 6, 7 and 8, which are digitized at 2 MHz, obtained during a single ELM. Peaks in the I_{SAT} signal during an ELM have been shown previously to be correlated with the arrival of filaments at the probe [6]. The filaments that are analysed are the ones that appear as prominent peaks with a similar temporal shape on pins 6, 7 and 8. Such a filament signal is the first peak (labeled I) shown in the traces of Figure 2. If it is not possible to observe the same profile on all three pins then the velocity is not calculated. For example, the shape of the second peak on pin 6 (labeled II) is different to that on pin 7 and 8 and so this peak is not analysed. One possible explanation for why different peaks are observed on the pins is that sometimes the filaments may split/divide upon interaction with the probe (typically more peaks are observed on pins 7 and 8 than on pins 1 and 6). Since the aim is to measure the velocity of the filament with which it propagated to the probe and not the velocity of filaments that may have broken up on interacting with the probe the analysis presented in this paper has required that a signal is observed on pins 1 6,7 and 8. Requiring that the signal has a similar temporal shape on each pin also reduces the problem of identifying the position of the centre of the peak. However, this selection may lead to some bias in the conclusions as only a subset of peaks are analysed.

Figure 3 shows a zoom in on the time interval around the filament labeled I in Figure 2. The first thing that can be noted is that the time of arrival of the first peak is different at pin 1 and pin 6. Even though pin 1 and 6 are at the same radial location they are not at the same poloidal location and the fact that the time of the first peak is different at the two pins indicates that the filaments still have a poloidal/toroidal rotation at the probe

location. Assuming the rotation is purely poloidal the rotation velocity in this example is 2 kms^{-1} in the ion diamagnetic direction (the mean poloidal velocity of all the filaments studied is 1.2 kms^{-1}). The poloidal velocity has been calculated for each filament and used to determine the radial velocity from pins 6,7 and 8 which are separated both radially and poloidally

Direct observation of the toroidal/poloidal motion of the filaments has been reported on ASDEX Upgrade using fast visible imaging [7]. These images show that the filaments start off rotating toroidally in the co-current direction (or poloidally downwards in the ion diamagnetic direction) and after some time the toroidal rotation of an individual filament slows and soon afterwards hits the limiter. The toroidal location has been fitted as a function of time to yield the initial toroidal velocity (which is in the range 10-30 kms^{-1}) and the toroidal deceleration (which is in the range $(1\text{-}5)\times10^{8}$ ms^{-2}). Taking into account the field line angle and the typical distances to the probe (5-10 cm) this corresponds to poloidal velocities in the range 0 to 4.0 kms^{-1} at the location of the probe, with a mean of 2kms^{-1} consistent with the measurement from the filament probe. On MAST the radial velocity of the filaments has also been determined from such images [8], however, on ASDEX Upgrade the field line angle at the mid-plane does not vary much with distance from the LCFS and so it is not possible to determine accurately the radial location of the filaments using such a technique. Only the mean radial velocity can be estimated using the time that a filament takes from appearing until it reaches the limiter. Filaments are observed for different periods of time, with a mean of 60 μs, before hitting the limiter (12 cm distant), which gives an estimate for the radial velocity of 2 kms^{-1}. If the filaments formed before

they became visible, that is they had to either cool sufficiently or to propagate radially into a region of sufficient neutral density before they became visible, then this would represent an upper limit on the velocity. On the other hand this could represent a lower limit if the filaments did not start to move radially until some time after they became visible. The implications of this will be compared to the velocities determined from the time delay on the probes in a later section.

The radial velocity has been determined from the filament probe signals for filaments in 490 ELMs from 12 discharges. Figure 4a shows a plot of the radial velocity (V_r) as a function of distance (ΔR_{LCFS}) from the Last Closed Flux Surface (LCFS). Since the probe location is fixed relative to the limiter, measurements have been made by changing the outboard edge of the plasma. It was not possible to make measurements at distances of $\Delta R_{LCFS} < 50$ mm due to the fact that either the signals saturated or substantial voltage drop occurred on the power supplies.

Figure 4a shows the probability density distribution of the radial velocities: there is a large scatter in the data with velocities between 300 and 3500 ms^{-1} being measured. Figure 4b shows a plot of the radial velocity as a function of ΔR_{LCFS}. In order to look for trends, the data have been binned as a function of ΔR_{LCFS}. In each bin the weighted mean and standard deviation have been calculated and these are shown superimposed on the plot as the squares and error bars respectively. The mean velocity is 1460 ms^{-1} and is effectively constant with distance from the LCFS over the region covered by the measurements ($40<\Delta R_{LCFS}<100$ mm). This is similar to what was reported in reference [5]. Over the limited radial extent measured there is no evidence that the filaments either accelerate or

decelerate, though presumably the filaments have to accelerate to 1500 ms^{-1} somewhere between the first measured point and the LCFS.

The discharges studied have a range of ELM frequencies with ELM energy losses (ΔW_{ELM}) 5 to 60 kJ. The ELM energy loss has been determined by measuring the drop observed in the diamagnetic energy (W_{MHD}) due to the ELM. Figure 5a shows V_r as a function of ELM energy. For a given ELM energy a large range of radial velocities are recorded. The data has again been binned, which shows that the mean value of V_r is constant with ELM energy loss. Previous works have suggested that the radial velocity may scale with ELM energy (see [9] and references therein). In particular, the interchange instability predicts that more intense filaments travel faster and that [10] $\frac{V_r}{c_s} \sim \sqrt{\frac{2\delta_\perp \Delta W_{ELM}}{R W_{ped}}}$ where c_s is the ion sound speed $\delta_\perp$ is the size of the filament, R the major radius and W_{ped} is the pedestal energy. Assuming that the filament size ($\delta_\perp$) does not change with the value of the ELM energy loss (ΔW_{ELM}) then such a model would predict that the radial velocity would scale as $\sqrt{\frac{\Delta W_{ELM}}{W_{ped}}}$. Figure 5b shows the measured radial velocity as a function of the fractional ELM energy loss $\Delta W_{ELM}/W_{ped}$. For a given fractional ELM energy loss a large range of radial velocities are recorded. The data has again been binned, which shows that the mean value of V_r is constant with $\Delta W_{ELM}/W_{ped}$.

Although there is no dependence of the radial velocity on the ELM size, similar to what was found in [5], V_r does depend weakly on the ion saturation current density (J_{SAT}) of the filaments (see Figure 6a). Shown on the plot are curves of the form $V_r \propto (J_{sat})^{\alpha}$ with

α = 0.5 (dashed) and 0.25 (dotted). As can be seen the measured dependence is much weaker than either of these. For filaments with the smallest values of J_{SAT} the mean value of V_r is ~ 1 kms^{-1} whereas for filaments with J_{SAT} > 10 kAm^{-2} the velocity is consistent with being a constant value of ~1.5 kms^{-1}. The correlation of the filament J_{SAT} with number of particles lost (Δn_e) during the ELM has been investigated. Although, it is more likely that filaments with a larger J_{SAT} are observed in ELMs with a large Δn_e there is no correlation of filaments with small J_{SAT} with small Δn_e. Hence this trend is not associated with the number of particles lost due to the ELM and, as has been seen on other devices, the fraction of particles lost is approximately constant with ELM size. It should be noted that since the J_{SAT} in the filaments decreases with distance from the LCFS, the filaments that have the smallest J_{SAT} are preferentially measured furthest from the plasma and so nearer to the limiter. It is not possible, from the current data set, to determine if the observed smaller velocities are due to features of the far SOL or the effect of the limiters rather than being due to a scaling of radial velocity with filament density (J_{SAT}).

Figure 6b shows a plot of V_r as a function of time in the ELM (t-t_{ELM}) where t_{ELM} is defined as the time of the peak in the target D_α light. There is a weak dependence of V_r on time in the ELM with a tendency for filaments detected at earlier times to have larger velocities than those at later times. This is similar to what has been observed on NSTX [12] where a large difference in velocities has been observed between early filaments (called primary filaments) and those observed at later times (called secondary filaments).

The Time Of Flight (TOF) radial velocity (V_{TOF}) of the filaments has been estimated previously on ASDEX Upgrade using the time difference between the start of the

rise time of the target D_α light (assumed to be due to the arrival of fast electrons released by the ELM event arriving at the target measured with an accuracy of ~ 20 μs) and the time of the peak in the I_{SAT} at the first probe as a function of distance from the LCFS [11]. This method has also been applied to the current data. Figure 7a shows a plot of the radial velocity calculated using the separated probes (V_r) compared to the time of flight velocity (V_{TOF}). As can be seen the values of V_{TOF} are much smaller than V_r. A similar effect has also been observed on MAST [3], where an analysis of images reveals that the reason for the discrepancy between the two results is due to the fact that the filaments do not all leave the LCFS at the same time and they do not begin to separate until 50-100 μs after the start of the rise in the D_α light. Hence the propagation time to the probe is over estimated and the subsequent value of V_{TOF} underestimated. The current data from ASDEX Upgrade can be used to estimate the time that the filaments leave the LCFS (t_{left}) defined as $t_{left} = \Delta R_{LCFS} / V_r$. Combining this with the start time of the ELM, defined as the start of the D_α rise at the target, the time that the filaments leave the LCFS relative to the start of the ELM (t_{delay}) can be calculated. Figure 7b shows the probability distribution of delay times, which shows that filaments leave the LCFS over a period of ~ 400 μs. What is interesting is that there appears to be two peaks one at ~ 100 μs and the other at ~ 250 μs. This could indicate that there really are primary and secondary filaments as suggested by NSTX [12].

3. Determining the radial velocity from ExB measurements

The radial velocity of the filaments is often determined assuming that their motion is due to an $\vec{E} \times \vec{B}$ drift. The poloidal electric field (E_ϑ) is then estimated by measurements of the floating potential from two poloidally separated probes and the radial velocity is calculated from $V_r = E_\vartheta / B$. In this section the difficulties in determining this quantity will be discussed.

The standard method to determine the poloidal electric field is to measure the floating potential V_{fl} at two Langmuir pins separated by a distance *d*. This measurement can be made with high time resolution and *E* is then approximated by $E = (V_{fl,1} - V_{fl,2})/d$. In fact the electric field is really the gradient in the plasma potential (ϕ_{pl}) $\phi_{pl} = V_{fl} - \alpha T_e$ where α~3 and T_e is the electron temperature. Changes in electron temperature are usually neglected, however, for a typical pin separation of 10 mm a difference in T_e of 1 eV at the two pins would modify the calculated electric field by 300 Vm^{-1} and the calculated radial velocity in a machine with a field of 2 T by 150 ms^{-1}.

The next problem is trying to determine how the large scale motion of the filament is related to the small scale turbulence occurring within the filament i.e. is the measured E_ϑ a measure of the local phase velocity of the turbulence within the filament or the group velocity of the filament as a whole? The values of V_r determined using this technique usually show large positive and negative fluctuations [13][14][15][16][17] presumably due to the fact that what is being measured is the local phase velocity of the turbulence rather than the net outward motion of the filaments. This would mean that the velocity determined

would be very sensitive to the location of the pins relative to the filament. In order to reduce these fluctuations some authors [14] have weighted the measured velocity by the measured ion saturation current i.e. $V_r = \langle I_{SAT} E_\vartheta \rangle_{dt} / \langle I_{sat} \rangle_{dt} B$, where the data is averaged over some period *dt*, which should presumably relate to the temporal width of the filament. The advantage of this method is that it gives more importance to the parts of the distribution that have the largest density (I_{SAT}) the disadvantage is that the time period over which to average is a free parameter. For example, in reference [14] the averaging is performed over a 100 μs time window.

Figure 8 shows a photograph of the high heat flux probe head which has been used for the studies presented in this paper. It is attached to the mid-plane manipulator on ASDEX Upgrade, which is located at the low field side about 31 cm above the magnetic axis. The head which is made of graphite consists of two columns each with 5 Langmuir pins each separated by 3mm. The tips are mounted in plane with the surrounding shield, analogous to flush-mounted probes in the divertor. The probe surface is tilted 14° with respect to the toroidal direction. For the discharges discussed here the probes are connected such that pins 1, 3 and 5 measure the floating potential and pin 4 measures the ion saturation current.

Figure 9 shows the traces observed on the probe during a single type I ELM in shot 23402 when the probe is located 6 cm from the LCFS and the plasma wall gap is greater than 10 cm at the closest point on the low field side. Figure 9a shows the target D_α and ion saturation current density (J_{SAT}) recorded by pin 4 as a function of time relative to the peak in the D_α intensity. Several peaks are observed in the J_{SAT} trace during the rise in the D_α

signal. Figure 9b shows a zoom in on the J_{SAT} signal during the rise time of the D_α light which shows at least 5 clear peaks, which are assumed to be due to the interaction of ELM filaments with the probe. Figure 9c shows the radial velocity calculated from the difference in floating potential on combinations of pins. The traces show V_r calculated using $V_r = (V_{fl}^i - V_{fl}^j)/(B \cdot d_{i,j})$ where i, j=3, 5 for the red 1, 3 for the blue and 1, 5 for the green traces respectively. Large values of V_r are produced, with V_r up to 3000 ms^{-1}, with the largest signals being in the vicinity of the peaks in the J_{SAT}. However, the magnitude and even the sign of V_r are dependent on the set of pins used. For example, although the sign of V_r is the same from pins 1, 5 and 3, 5 the signal from the latter set is consistently larger by up to a factor of 2. The sign of the signal from pins 1, 3 is often opposite to that from pins 3, 5. Figure 9d shows the radial flux calculated from V_r and the J_{SAT} signal assuming a temperature of 20 eV. As for the velocity the flux also depends strongly on the set of pins used. Even over the time period shown the integrated flux is different with $\int \Gamma_{i,j} dt$ being 0.021 (pins 3, 5), 0.0018 (pins 1, 3) and 0.011 (pins 1, 5) m^{-2}.

In order to investigate this effect further a synthetic diagnostic, representing the probe head used in ASDEX Upgrade, has been inserted into the TOKAM-2D interchange turbulence simulation code [18][19], simulating an L-mode like plasma. The turbulent flux has been calculated using spatially separated probe pins sampling the plasma potential and density. This is more favorable than in the experiment since the probes directly measures the quantities of interest for calculating the flux. This means that the fluxes calculated by this synthetic probe are not distorted by any electron or ion temperature fluctuations. The radial particle flux has been calculated for probes with varying separations and for either

the density measuring probe in the centre of the two plasma potential probes (i.e. like the V_{fl}^3-J_{SAT}^4-V_{fl}^5 or the V_{fl}^1-J_{SAT}^4-V_{fl}^5 combination used in the experiment) or with the density measuring probe outside the two plasma potential probes (as in the V_{fl}^1-V_{fl}^3-J_{SAT}^4 combination). The flux has been determined at a position near to the LCFS and integrated over the simulation time period of 2.6 ms. The flux has been calculated with varying spacing of the probes measured in units of the ion gyro-radius (ρ_i). The mean radial flux calculated as a function of probe separation, normalized such to the value at zero pin separation, is shown in Figure 10.

Similar to what was observed experimentally a large difference is found in the fluxes depending on the probe arrangement and both negative and positive fluxes are calculated. The smallest dependence on pin separation is obtained for the case when the density measuring probe is in the middle of the two ϕ_{fl} probes. In the experiment the exact value of ρ_i depends on the temperature of the filaments when they reach the probe. In reference [5] it was estimated that typical values for the filaments in the far scrape off layer of ASDEX Upgrade are Te=5 eV and Ti=30-60 eV. Recent measurements using a fast swept probe [20] has recorded electron temperature due to filaments of up to 40 eV and measurements from a Retarding Field Analyser [21] have indicated Ti up to 100 eV. Hence the pin to pin separation of 3mm (i.e. pin 1 to pin 2) in the experiment corresponds to ~5-9 ρ_i, which is shown as a horizontal line in Figure 10. For such pin separations the arrangement "V_{fl}^3-J_{SAT}^4-V_{fl}^5" has least dependence on the pin separation and results in a calculated flux of ~ 90 % of the radial flux at zero pin separation. Similar to what is observed experimentally the flux calculated using the "V_{fl}^1-J_{SAT}^4-V_{fl}^5" combination results

in fluxes of ~ 50 % of the flux measured by the "V_{fl}^3-J_{SAT}^4-V_{fl}^5" combination. Finally the flux calculated from the "V_{fl}^1-V_{fl}^3-J_{SAT}^4" combination is much smaller again similar to the experimental findings. It should be stressed that these simulations are presented to show the large differences that can be obtained with different probe configurations and not to try to prove that the radial velocities measured by the "V_{fl}^3-J_{SAT}^4-V_{fl}^5" combination is correct. In fact there are several things that are missing from the current simulations that would need to be included in future simulations. Firstly, the simulations are in an isothermal plasma so temperature gradients in the poloidal direction are not considered and hence $\nabla V_{fl} \sim \nabla \phi_{pl}$. In an ELM filament there is likely to be significant temperature gradients present and the edge effects relative to the underlying plasma background are likely to be larger. In the simulations the measurements are instantaneous, whereas the experimental data is obtained over some acquisition time. The effect of this experimentally is described below.

Figure 11 shows the effect of the choice of pins and integration period on the radial velocity calculated using the method described above and in [14][15], which is based on weighting the velocity with the ion saturation integrated over a certain time period. Figure 11a shows the J_{SAT} signal and Figure 11b V_r from pins 3,5. The radial velocity is calculated as $V_r = \langle J_{SAT} E_\vartheta \rangle_{dt} / \langle J_{sat} \rangle_{dt} B$ and has been calculated for values of *dt* of 0.5 (black) 5 (red) 20 (blue) and 50 (green) μs. Note: *dt*= 0.5 μs means no integration is done as this represents the digitization time of the probes and hence in this case $V_r = E_\vartheta / B$ and the curve is identical to the equivalent one shown in Figure 9c. As expected the effect of

increasing the integration period is to smooth out the peaks in the distribution and hence to reduce the peak velocity associated with each filament.

In order to investigate the effect the choice that the time integration period has on the radial velocity, V_r has been calculated at each peak in the ion saturation current for a set of 680 ELMs from a variety of discharges, which produced 1720 individual measurements. Figure 12 shows the probability distribution obtained. For the different integration times *dt* = 0.5, 5, 20, 50 μs the mean value of V_r obtained is $\langle V_r \rangle$ = 1145, 847, 489, 359 ms^{-1} respectively. All of these velocities are significantly less than was measured using the two radially separated probes presented in the section 2.

It is difficult to justify any choice of integration time; however, the integration time should probably be less than the filament extent. The mean temporal width of the J_{SAT} signal is ~ 5 μs duration [5], which should be the upper limit for the integration time. In the following, an integration time of 5μs has been used in order to smooth out some of the largest fluctuations. However, there is no difference in the trends presented if no integration was used; the only effect is in the magnitude of V_r which is ~ 1.5 times larger in the case of no integration.

Figure 13a shows the radial velocity determined in this way as a function of the distance (ΔR_{LCFS}) of the probe from the Last Closed Flux Surface (LCFS). There is a large spread in the data with values of between -500 and 3000 ms^{-1} being measured over the entire radial distance considered. It is possible that there are fewer events at the largest velocities at larger distances. The data have been binned as a function of ΔR_{LCFS} and in each bin the weighted mean and standard deviation calculated, which are shown

superimposed on the plot as the squares and error bars respectively. The mean velocity of ~ 850 ms^{-1} is effectively constant with distance from the LCFS. This trend is similar to what was observed in JET [22], although in the JET case the radial velocity is smaller (~ 100 ms^{-1}), which may be due to the longer integration time used (100 μs) in that study.

Figure 13b shows the V_r as a function of ELM size. The ELM size varies in the discharges considered from 5 kJ up to 60 kJ while the ELM frequency varies from 400 Hz to 30 Hz. Similar to what was found from the filament probe data presented in section 2 there is little evidence that the mean value of the velocity changes with ELM size. On JET, for ELM frequencies less than 100 Hz there is also very little change of V_r with ELM frequency and presumably size [15], however, for ELM frequencies above 200 Hz there is a large reduction in the average radial velocity.

Figure 13c shows *Vr* as a function of time from the peak in the target D_α intensity. The mean velocity is marginally higher at early times in the ELM but the effect is much smaller than was found from the filament probe data. Finally, Figure 13d shows *Vr* as a function of the size of the J_{SAT} signal corresponding to the ELM filament. V_r is approximately constant for J_{SAT} greater than ~ 20 kAm^{-2}. Similar to what was found from the filament probe data, filaments that have small values of J_{SAT} have a smaller value of V_r. On JET it was also found that the radial velocity increases with the size of the ion saturation current [14].

4. The relationship between radial velocity and the ion saturation radial fall off length

Rather than reporting individual filament motion the radial expansion of the filaments is often captured in terms of a radial e-folding length of particles and energy. Measurements of the peak value of the ion saturation current as a function of distance from the LCFS have been made using the Langmuir probe located on the high heat flux probe described in section 3. The ion saturation current e-folding length (λ_{ISAT}) has been determined for 14 shots with a range of plasma parameters including ELM size and pedestal temperature which have been produced by changing the density and/or the injected beam power.

Figure 14 shows ion saturation current radial profiles on a log-linear plot. Figure 14a shows the distribution obtained during the reciprocation of the probe, which occurred during a period of the shot with approximately constant parameters. The mean and standard deviation of ELM energy loss for the 239 ELMs measured during the reciprocation is ΔW_{ELM} = 4±1 kJ. A fit to the distribution yields λ_{ISAT}=25±2 mm. Figure 14b shows the distribution from a shot with 50 ELMs analysed with ΔW_{ELM} = 21±4 kJ, which has λ_{ISAT}=18±3 mm.

In the simplest picture where the filaments propagate out radially with a constant velocity (V_r) and lose particles on ion parallel transport timescales ($\tau_{//} = L_{//}/c_s$, $L_{//}$ is the connection length and c_s the ion sound speed) then the particle e-folding length (λ) can be expressed as $\lambda \sim V_r \tau_{//} \sim V_r L_{//}/c_s$. If this expression is correct, and using the findings in the previous sections that V_r is independent of ELM size, then the ratio of the e-folding lengths

in two discharges would be $\lambda^a/\lambda^b = \left(L^a_{//}/c^a_s\right)\Big/\left(L^b_{//}/c^b_s\right)$. Assuming that the value of the ion sound speed scales with the temperature pedestal (i.e. $c_s \propto \sqrt{T^{ped}}$) and using the parameters of the discharges shown in Figure 14a and b respectively, then the RHS of the equation is 1.6±0.2 which is in agreement with the ratio of the e-folding lengths of 1.4±0.2. Whilst the ratio is in good agreement the absolute value does not work, for example, for the discharge shown in Figure 14a the values are $L_{//}$=15 m, c_s = 1.8x10^5 ms^{-1} (for a T^{ped} = 350 eV and assuming T_e=T_i) and V_r= 1500 ms^{-1} then $\lambda \sim V_r L_{//}/c_s$ ~125 mm, which is much larger than the measured e-folding length. If instead the 5 μs smoothed $\vec{E}\times\vec{B}$ velocity of ~ 850 ms^{-1} from the previous section is used, which is most likely an underestimate of the radial velocity, then the e-folding length ($\lambda \sim 70$ mm) is nearer but still larger than the measured one. One of the reasons for the discrepancy is that C_s is not a fixed quantity but varies with distance from the LCFS. Also $L_{//}$ may not be the best measure of how quickly the particles content at the mid-plane changes with time and distance. Instead it may be better to use the length of the filament at the time it leaves the LCFS and this is a smaller distance than $L_{//}$. In order to take these features into account a simulation is required.

In order to get a better understanding of how the radial motion of, and parallel transport within, a filament gives rise to the observed radial decays a Monte Carlo simulation has been performed using the method described in reference [2]. The filament is assumed to be born with a length 2X, where X is taken as the length along the field line 1cm outside the LCFS between the mid-plane and a point above the lower X-point. This point is defined as the height of the lowest point of the 95 % flux surface. Initially this

filament is uniformly populated with particles, each of which has a velocity as derived from a Maxwellian velocity distribution according to an initial temperature and it is assumed that ion parallel transport is dominant. Each particle is tracked until it leaves the end of the filament. Such a simulation has previously been able to successfully describe the target profiles and the fraction of power arriving at the targets on MAST [23] and ASDEX Upgrade [7]. In the present simulations the number of particles and the mean absolute velocity of the particles within ±0.1 X of the centre of the filament are calculated to represent the density and ion temperature at the mid-plane of the filament. In all the simulations the radial velocity has been kept constant at V_r= 1500 ms^{-1}. Figure 15 shows the ion saturation current calculated from these values as a function of distance from the LCFS over the radial distance measured by the mid-plane probe. Figure 15a shows the simulation for the parameters similar to shot 21302 (Figure 14a) namely: T^{ped} = 350 eV and q_{95} = 5.5, which has an e-folding length λ = 24 mm. Figure 15b shows the simulation for the parameters similar to shot 23394 (Figure 14b) namely T^{ped} = 600 eV and q_{95} = 4.6 which has an e-folding length λ = 19 mm. Both simulated distribution have e-folding length close to the measured values.

The simulations presented in Figure 15 would represent the case where all the filaments had the same density and radial velocity. The filaments detected during similarly sized ELMs at fixed distance to the LCFS have a range of ion saturation currents and hence densities and the simulations have been used to investigate the effect of this has on the e-folding lengths measured. In some discharges the probe was held at constant distance from the plasma for an extended period of time (up to 200 ms) in order to determine the

distribution of ion saturation currents. Figure 16a shows the probability distribution function from two such shots which had different plasma parameters. So that the distributions can be overlaid the ion saturation current has been normalised to the mean in each case and the spread in each distribution is found to be similar. This has been used as input to the simulations where filaments are generated with a range of densities distributed according to this measured distribution. In the original simulation each filament generated initially had 1 million particles in it. In the following simulations 100 filaments are generated each having an initial number of particles distributed according to the fractional density shown in Figure 16b i.e. 8 filaments are generated with 1 million particles, 5 have 0.5 million, another 5 have 1.5 million etc.

Two simulations have been performed, one assuming that Vr is independent of density and the other assuming that the radial velocity scales with the initial filament density as $V_r \propto \sqrt{n_{fil}}$, with V_r=1.5kms^{-1} when $n_{fil} = 1$. The velocity distribution implied by this scaling is shown as the dashed curve in Figure 16c. This velocity distribution bears little similarity to the one measured experimentally (Figure 4a). However, this distribution would only be obtained if the time delay between the two probes could be determined infinitely accurately (i.e. $t_{delay} = d/V_r$, where d is the distance between the probes). In reality there is an uncertainty (δt) associated with the accuracy with which the time delay can be measured. This would result in a measured velocity $V_r^{'} = d/(t_{delay} + \delta t)$. Assuming this uncertainty is uniformly distributed in the range ±0.5 μs, which is the accuracy to which the time delay from the filament probe can be measured, then the velocity distribution that would be measured experimentally is shown as the solid curve in Figure

16c, which is in much better agreement with the data (Figure 4a). Hence although there is no direct evidence that $V_r \propto \sqrt{n_{fil}}$, using such a parameterisation allows the spread in radial velocities to be captured in the simulations.

The parameters used in the simulation are the same as those used in Figure 15a i.e.: T^{ped} = 350 eV and q_{95} = 5.5. The resulting ion saturation current radial profile that would be measured is shown in Figure 17a assuming that the radial velocity of each filament is independent of density and in Figure 17b assuming that the radial velocity scales as $V_r \propto \sqrt{n_{fil}}$. In both cases the e-folding lengths measured are similar to those assuming all the filaments have equal density and there is little difference between the two radial velocity assumptions.

In a typical experimental set of radial profiles the ion saturation current is measured from~ 100 ELMs. Therefore in the simulation 100 points have been chosen at random from the underlying distribution and the new distribution fitted. An example of a randomly selected sample for the case where $V_r \propto \sqrt{n_{fil}}$ in shown in Figure 17c. The fit to the distribution gives an e-folding length λ=24.1±2.4 mm. The error bar is similar to that obtained from the fits to the experimental data. This random selection of the data has been repeated 100 times and each distribution fitted to determine the e-folding length. Figure 17d shows the distribution of the resulting e-folding lengths for the two radial velocity assumptions. The distribution has a mean of 23.1 (22.1) and standard a deviation of 1.7 (2.8) for the V_r constant ($V_r \propto \sqrt{n_{fil}}$) cases respectively. These results indicate that a representative measurement of the e-folding length can be made from a collection of

individual filaments where each filament gives just one measurement i.e. a value of J_{SAT} at a given distance. This is true even if the filaments have a range of initial densities and the result is moderately insensitive to the way that the filament velocity scales with initial density. The uncertainty in the measured e-folding length varies with the number of points in the distribution but 100 points gives a reasonable level of accuracy.

Figure 18a and b show the e-folding length measured in 14 discharges in which at least 100 points were measured in the radial J_{SAT} distribution as a function of ELM energy loss (ΔW_{ELM}) and fractional ELM energy loss ($\Delta W_{ELM}/W_{ped}$). In both cases there is a large scatter in the data but there is no noticeable trend i.e. there is no evidence that $V_r \propto \sqrt{\Delta W_{ELM}}$ or $V_r \propto \sqrt{\Delta W_{ELM}/W_{ped}}$. The different sized ELMs have been achieved by varying plasma parameters such as T^{ped} and q_{95} ($L//$) and as shown earlier these can have an influence on λ. Figure 18c shows a plot of the measured λ versus λ_{scale} defined as $\lambda_{scale} = V_r L_{//}/c$ calculated using the parameters from each discharge and assuming V_r=1.5 kms^{-1}. The magnitude of the numbers does not agree but a clear correlation is observed between the measurements and the scaling. In order to investigate any underlying dependence of the e-folding length on the ELM size the measured λs have been normalised by this scaling. Figure 18d shows that the normalised λs are effectively constant as a function of the fractional ELM energy loss ($\Delta W_{ELM}/W_{ped}$). This is consistent with the previous measurements that V_r is independent of ELM size.

5. Summary and Discussions

The radial propagation of type-I ELMs in ASDEX Upgrade has been measured using a number of techniques. In principle the most reliable technique should be to use the time delay between two radially separated probes. The limitation of this method is that although the probes are close together poloidally they still may sample a different part of the filament. Any internal density structure within the filament may result in different peaks being observed on the different probes and in fact, often the temporal signature on all 3 probes is not the same. In the analysis presented here only those filament where the temporal trace on the 3 probes is similar has been analysed. The measurements can be used to extract a mean poloidal velocity of 1.2 kms^{-1} and a mean radial velocity obtained of ~1.5 kms^{-1}. The poloidal velocity measured is in good agreement with previous measurements using visible imaging [7]. In order to determine the radial velocity from imaging the system would need to be improved with more localised measurements of the filaments, possibly viewing along the magnetic field line as has been done in gas puff imaging on other devices [12].

The radial velocity was also calculated using a time of flight technique based on measuring the arrival of filaments at a single probe relative to an ELM start time assumed to be the time of the start of the rise of the divertor D_α. These measurements give a mean radial velocity of ~ 250 ms^{-1}, which is a factor of 3-4 time smaller than the value of Vr determined from the filament probe for the same filaments (see Figure 7a). The reason for the discrepancy is due to the in correct assumption on the start time. In fact, the filament

probe data shows that all filaments do not leave the LCFS at the start of the ELM but rather leave over a period of up to 400 μs.

The next method presented was to try to determine the $\vec{E} \times \vec{B}$ velocity by measuring the floating potential at two poloidally separated probes. Although probably the easiest measurement to make this method has the largest uncertainties associated with it. Any differences in temperature at the two probes is ignored, this can have large implications on the derived value of the poloidal electric field. Even if the gradient in the plasma potential was measured there would still be the question of whether the measurement was of the local turbulence or of the overall radial motion of the filament. The results obtained are very sensitive to the location of the probes used and any smoothing or time averaging that is performed, with the smoothing reducing the radial velocity calculated. The mean radial velocity calculated is ~ 1100 ms^{-1} for a smoothing of 0.5 μs (the data acquisition time) decreasing to ~ 850 ms^{-1} for a 5μs smoothing.

In spite of the differences in the size of the mean radial velocity from the filament probe and the floating potential measurements the over all trends with plasma parameters are similar. The results suggest that V_r is independent on distance from the LCFS in the range ($20<\Delta R_{LCFS}<100$ mm) and on ELM size but may depend on J_{SAT} especially for small values of J_{SAT}. The dependence of V_r on J_{SAT} would imply that the radial velocity depends on the initial filament J_{SAT} and not on the local or "time evolving" filament J_{SAT} since if V_r depended on the local J_{SAT} then the radial velocity would decrease with distance from the plasma as the particle content and temperature within the filament decreases, which is not

observed. Since $J_{SAT} \propto n_e\sqrt{T}$ it is difficult to determine whether this is an initial density or temperature effect.

The final method used to determine the radial propagation was a measurement of the ion saturation current e-folding length. A simulation shows that although the e-folding is extracted from many individual filaments it can still be used to determine the characteristics of the filament propagation. The e-folding length scales with q_{95} ($L_{//}$) and inversely with the square root of the temperature pedestal ($1/c_s$). Once these dependencies are accounted for the evolution of the e-folding length with $\Delta W_{ELM}/W_{ped}$ is consistent with V_r being independent of ELM size.

Acknowledgement

This work was partly funded by the United Kingdom Engineering and Physical Sciences Research Council under grant EP/G003955 and by the European Communities under the contract of Association between EURATOM and CCFE. The views and opinions expressed herein do not necessarily reflect those of the European Commission.

References

[1] Loarte A *et al.* 2002 *Plasma Phys. Control. Fusion* **44** 1815

[2] Kirk A *et al.* 2009 *J. Nucl. Mater.* **390-391** 727

[3] Kirk A *et al.* 2008 *J. Phys.: Conf. Ser*. **123** 012011

[4] Loarte A. *et al.* 2008 " Power and particle fluxes at the plasma edge of ITER : Specifications and Physics Basis", Proc. 22nd IAEA Fusion Energy Conf, (Geneva) IAEA-CN-165/IT/P6-13

[5] Schmid A *et al.* 2008 *Plasma Phys. Control. Fusion* **50** 045007

[6] Kirk A *et al.* 2004 *Phys. Rev. Lett.* **92** 245002

[7] Kirk A *et al*. 2008 *J. Phys.: Conf. Ser*. **123** 012012

[8] Kirk A *et al.* 2006 *Phys. Rev. Lett.* **96** 185001

[9] Loarte A et al. 2006 ELMs and disruptions in ITER : Expected Energy Fluxes on Plasma-Facing Components from Multi-machine Experimental Extrapolations and Consequences for ITER Operation" Proc of 21st IAEA Fusion Energy Conf, (Chengdu) IAEA-CN-149/IT/P1-14

[10] Garcia O E *et al.* 2006 *Physics of Plasmas* **13** 082309

[11] Kirk A *et al*. 2005 *Plasma Phys. Control. Fusion* **47** 995

[12] Maqueda R *et al.* 2009 *J. Nucl. Mater.* **390-391** 843

[13] Rudakov N L *et al.*, 2002 *Plasma Phys. Control. Fusion* **44** 717

[14] Goncalves B. *et al*. 2003 *Plasma Phys. Control. Fusion* **45** 1627

[15] Silva C. *et al.,* 2005 *J. Nucl. Mater.* **337-339** 722

[16] Endler M *et al*. 2005 *Plasma Phys. Control. Fusion* **47** 219

[17] Ionita C *et al.,* 2009 J. Plasma Fusion Res. SERIES **Vol. 8** 413

[18] Sarazin Y. and Ghendrih P. 1998 *Phys. Plasmas* **5** 4214

[19] Sarazin Y *et al*. 2003 *J. Nucl. Mater.* **313-316** 796

[20] Muller H.W. at al., Towards fast electron temperature measurements using swept Langmuir probes To be published in Contributions to Plasma Physics

[21] Kocan M. et al. "Measurements of ion energies in the AUG tokamak plasma boundary" To be submitted to *J. Nucl. Mater.*

[22] Silva C. *et al.,* 2009 *J. Nucl. Mater.* **390-391** 355

[23] Kirk A et al. 2007 *Plasma Phys. Control. Fusion* **49** 1259

6. Figures

Figure 1 Position and mapping of the filament probe pins in the radial–poloidal plane for a shot with a field line inclination angle of 8.6°. The insert shows a photo of the probe head and the location of the pins used.

Figure 2 a) The target D_α signal and the ion saturation current traces for b) pin 1, c) pin 6, d) pin 7 and e) pin 8 during an ELM as a function of time relative to the peak of the diverter D_α signal (t_{ELM}).

Figure 3 The ion saturation current traces for a) pin 1, b) pin 6, c) pin 7 and d) pin 8 during the ELM shown in relative to the first peak in the ion saturation current on pin 1 (t_{Ipeak}).

Figure 4 a) The probability distribution function for the radial velocity (V_r) determined from the time delay between the ion saturation current peaks from the filament probe. b) V_r as a function of distance from the last closed flux surface (ΔR_{LCFS}). The open squares and associated error bars superimposed on the plot represent the weighted mean and standard deviation calculated in bins of ΔR_{LCFS}.

Figure 5 The radial velocity (V_r) determined from the time delay between the ion saturation current peaks from the filament probe a) as function of ELM energy loss (ΔW_{ELM}) and b) as a function of ELM energy loss normalised to the pedestal energy ($\Delta W_{ELM}/W_{PED}$). The open squares and error bars represent the binned mean and standard deviation of the distribution.

Figure 6 The radial velocity (V_r) determined from the time delay between the ion saturation current peaks from the filament probe a) as function of ion saturation current density (J_{SAT}) at the first probe and b) as a function of time relative to the peak of the diverter D_α signal (t_{ELM}). The open squares and error bars represent the binned mean and standard deviation of the distribution. The curves in a) represent a dependence of the form $V_r \propto (J_{sat})^\alpha$ with $\alpha = 0.25$ (dotted) and $\alpha = 0.5$ (dashed).

Figure 7 a) The radial velocity (V_r) determined from the time delay between the ion saturation current peaks from the filament probe versus the velocity determined form the time delay between the start of the ELM and the peak in the ion saturation current at the probe (V_{TOF}). b) The probability distribution function for the time delay between the start of the ELM and the filaments starting to move radially, assuming a constant radial velocity with distance.

Figure 8 Probe head on reciprocating probe showing the location of the pins which can be used to measure either floating potential or ion saturation current. The pins measure 2 mm by 4.13 mm and the separation between the centre of the pins in the vertical direction is 5 mm.

Figure 9 a) The ion saturation current (J_{SAT}) and the target D_α signal during an ELM as a function of time relative to the peak of the diverter D_α signal (t_{ELM}). b) the ion saturation current. c) the radial velocity ($E_\theta \times B/B^2$) and d) the particle flux (Γ) as function of time in the ELM calculated using the floating potential measurements from tips 3 and 5 (red curve), 1 and 3 (blue curve) and 1 and 5 (green curve).

Figure 10 Calculated mean normalised radial flux as a function of pin separation obtained by using a synthetic probe diagnostic in a TOKAM-2D simulation and calculating the plasma potential and density for different probe configurations similar to that used in the experiment namely: V_{fl}^3-J_{SAT}^4-V_{fl}^5 (circles), V_{fl}^1-J_{SAT}^4-V_{fl}^5 (triangles) and V_{fl}^1-V_{fl}^3-J_{SAT}^4 (squares). The horizontal line shows the range of pin separations in the experiment.

Figure 11 a) The ion saturation current as a function of time in the ELM and b) the time averaged ion saturation current weighted radial ($E_\theta \times B/B^2$) velocity using tips 3 and 5. The curves are for time averaging over 0.5 (black), 5 (red), 20 (blue) and 50 (green) μs.

Figure 12 The probability density function of the time averaged ion saturation current weighted radial velocity ($E_\theta \times B/B^2$) using tips 3 and 5 for time averaging over 0.5 (solid), 5 (dashed), 20 (dotted) and 50 (dashed-dotted) μs.

Figure 13 The time averaged ion saturation current weighted radial ($E_\theta \times B/B^2$) velocity using tips 3 and 5 for time averaging over 5 μs as a function of a) the distance from the last closed flux surface (ΔR_{LCFS}), b) ELM energy loss (ΔW_{ELM}), c) time relative to the peak of the diverter D_α signal (t_{ELM}) and d) ion saturation current density (J_{SAT}). The open squares and error bars represent the binned mean and standard deviation of the distribution.

Figure 14 The peak ion saturation current of the ELM efflux observed at the mid-plane manipulator as a function of distance from the last closed flux surface (ΔR_{LCFS}) for shots with a) T_e^{ped} = 350 eV , q_{95} = 5.5 and ΔW_{ELM} = 4 kJ and b) T_e^{ped} =600 eV, q_{95} = 4.5 and ΔW_{ELM}=21 kJ. The solid curves represent the result of an exponential fit to the data to determine the e-folding length (λ).

Figure 15 The radial distributions of ion saturation current at the mid-plane for simulated filaments moving with a constant radial velocity of 1.5 km s^{-1} with plasma parameters of a) T_e^{ped} = 350 eV , q_{95} = 5.5 and b) T_e^{ped} =600 eV, q_{95} = 4.5. The solid curves represent the result of an exponential fit to the data to determine the e-folding length (λ).

Figure 16 a) The probability distribution of the peak ion saturation current obtained during ELMs normalised to the mean obtained when the probe was at a fixed distance from the last closed flux surface for shot 23403 (solid) and 23404 (dashed). b) the probability distribution of the fraction of particles initially in each filament used in the simulations. c)

The probability distribution of the velocities assuming that $V_r \propto \sqrt{n_{fil}}$ assuming perfect measurements of the time delay (dashed) and including realistic errors (solid).

Figure 17 The radial distributions of ion saturation current at the mid-plane for simulated filaments having a range of densities moving with a) constant radial velocity of 1.5 km s^{-1} and b) assuming $V_r \propto \sqrt{n_{fil}}$. c) The radial distribution for 100 randomly selected events from the distribution in b). The solid curves represent the result of an exponential fit to the data to determine the e-folding length (λ). d) The probability distribution of the e-folding length measured by fitting 100 randomly selected distributions assuming constant velocity (solid) and $V_r \propto \sqrt{n_{fil}}$ (dashed).

Figure 18 The ion saturation current e-folding length (λ_{JSAT}) as a function of a) ELM energy loss (ΔW_{ELM}), b) ELM energy loss normalised to the pedestal energy ($\Delta W_{ELM}/W_{PED}$) and c) an e-folding length scaling ($\lambda_{scale} = V_r L_{//}/c$). d) λ_{JSAT} normalised by λ_{scale} as a function of ELM energy loss normalised to the pedestal energy.

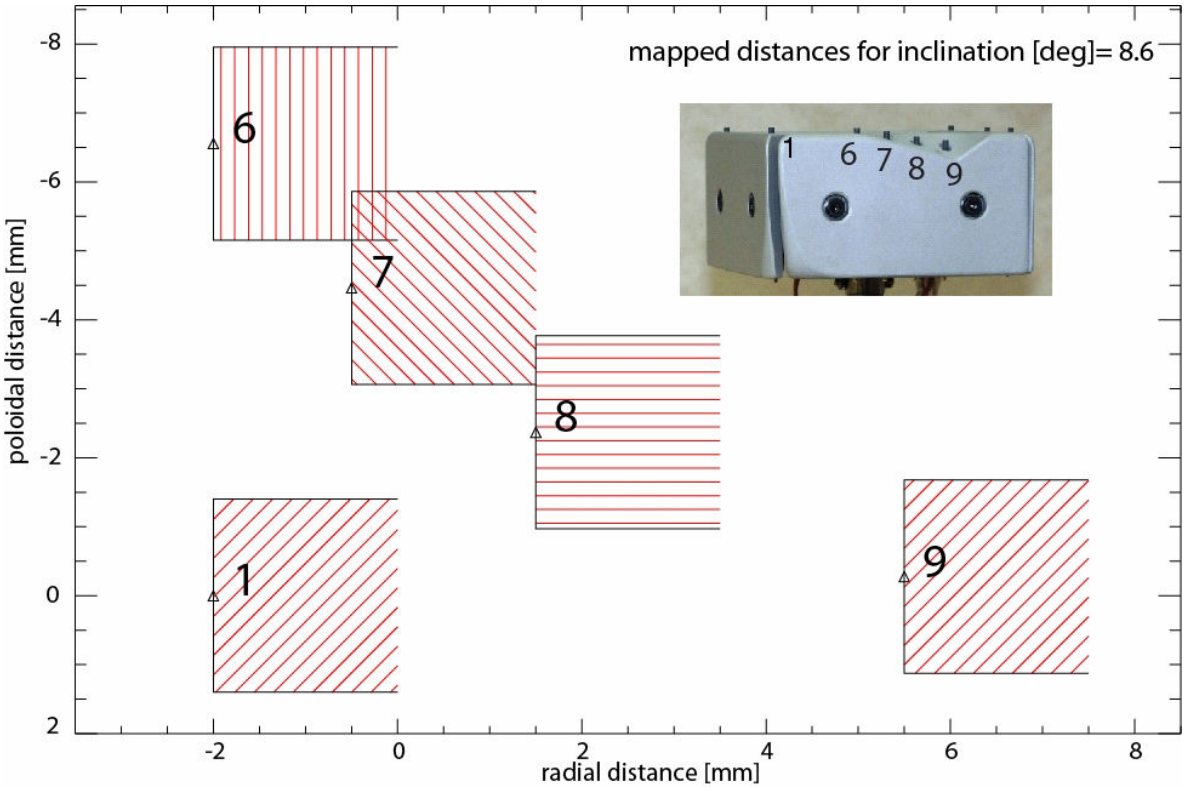

Figure 1 Position and mapping of the filament probe pins in the radial–poloidal plane for a shot with a field line inclination angle of 8.6°. The insert shows a photo of the probe head and the location of the pins used.

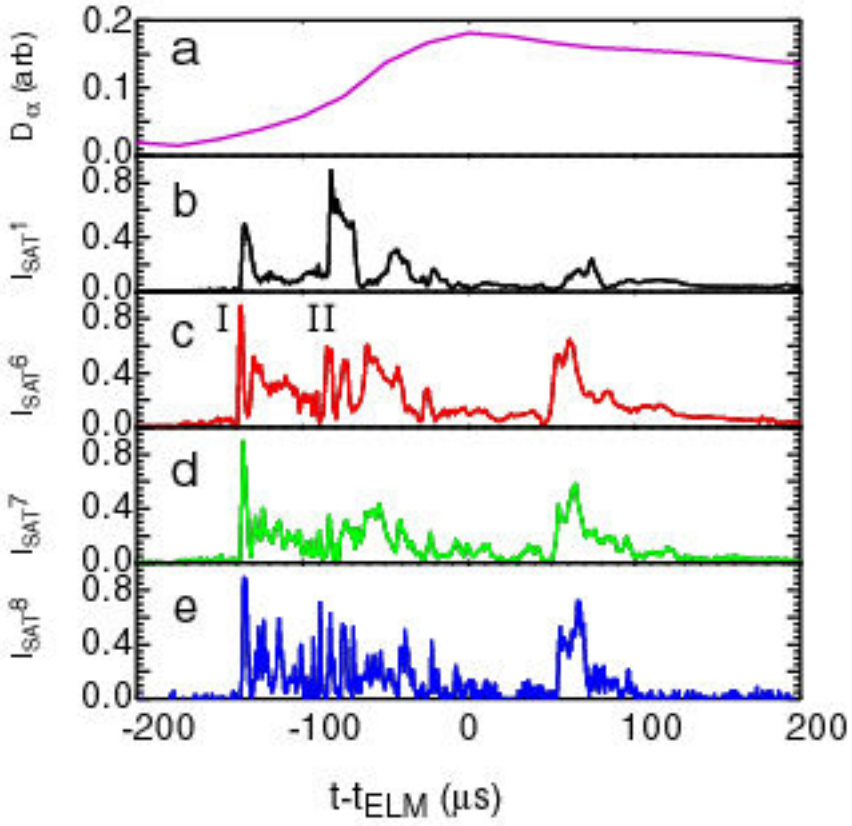

Figure 2 a) The target D_α signal and the ion saturation current traces for b) pin 1, c) pin 6, d) pin 7 and e) pin 8 during an ELM as a function of time relative to the peak of the diverter D_α signal (t_{ELM}).

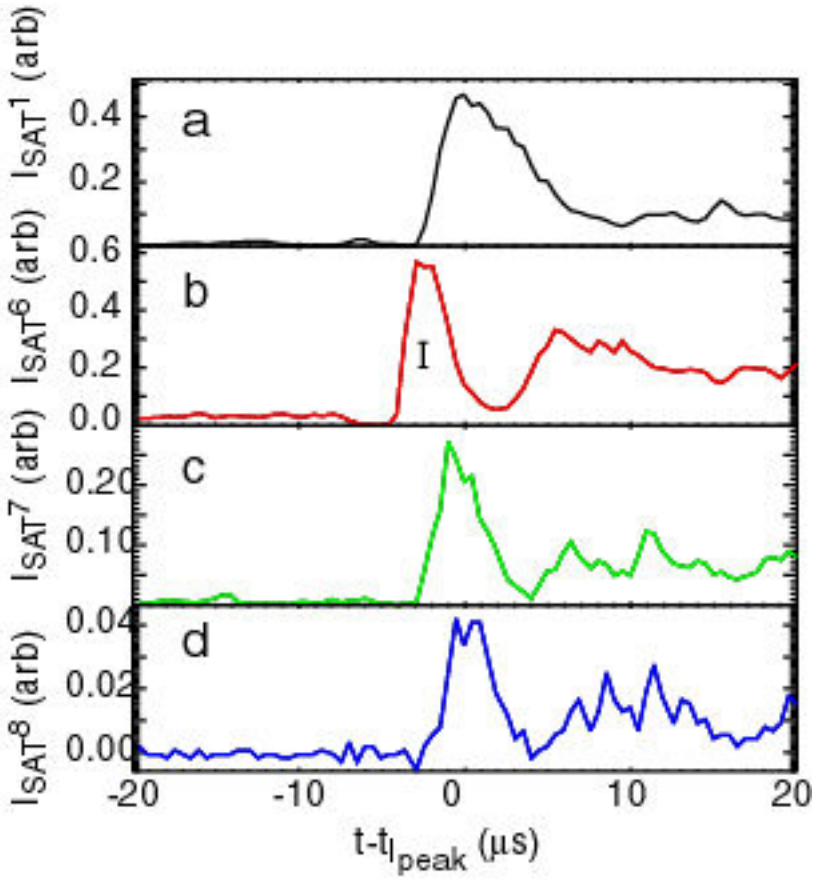

Figure 3 The ion saturation current traces for a) pin 1, b) pin 6, c) pin 7 and d) pin 8 during the ELM shown in relative to the first peak in the ion saturation current on pin 1 ($t_{I_{peak}}$).

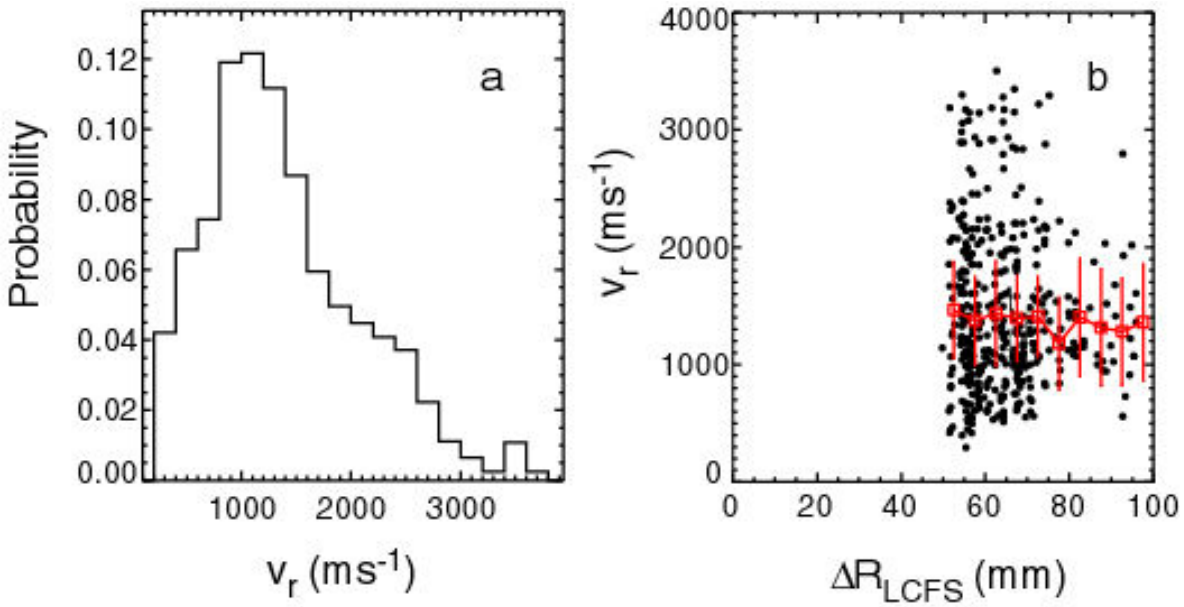

Figure 4 a) The probability distribution function for the radial velocity (V_r) determined from the time delay between the ion saturation current peaks from the filament probe. b) V_r as a function of distance from the last closed flux surface (ΔR_{LCFS}). The open squares and associated error bars superimposed on the plot represent the weighted mean and standard deviation calculated in bins of ΔR_{LCFS}.

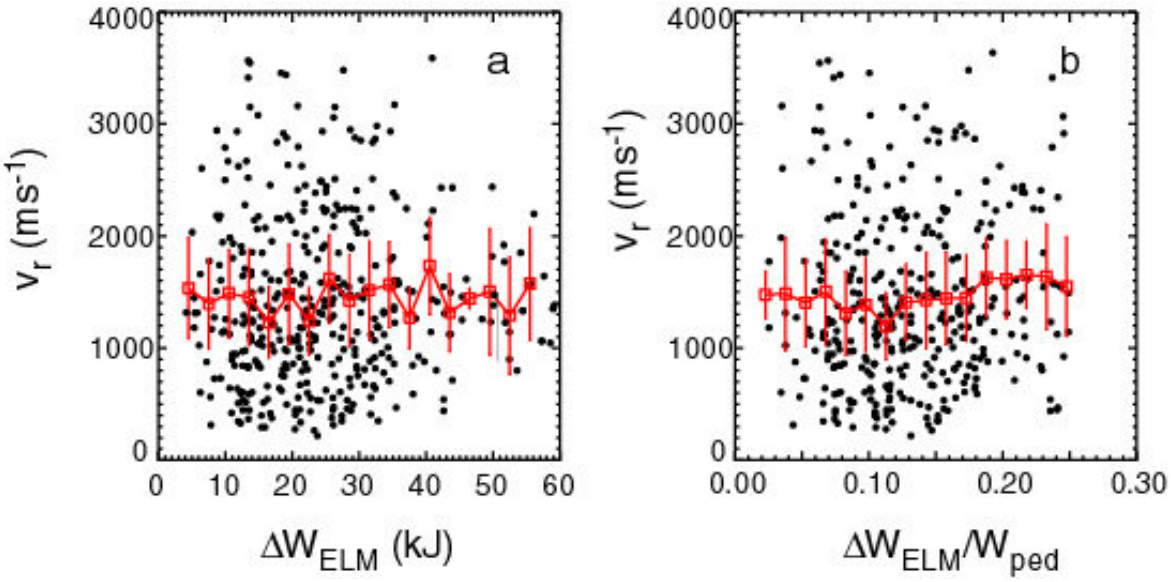

Figure 5 The radial velocity (V_r) determined from the time delay between the ion saturation current peaks from the filament probe a) as function of ELM energy loss (ΔW_{ELM}) and b) as a function of ELM energy loss normalised to the pedestal energy ($\Delta W_{ELM}/W_{PED}$). The open squares and error bars represent the binned mean and standard deviation of the distribution.

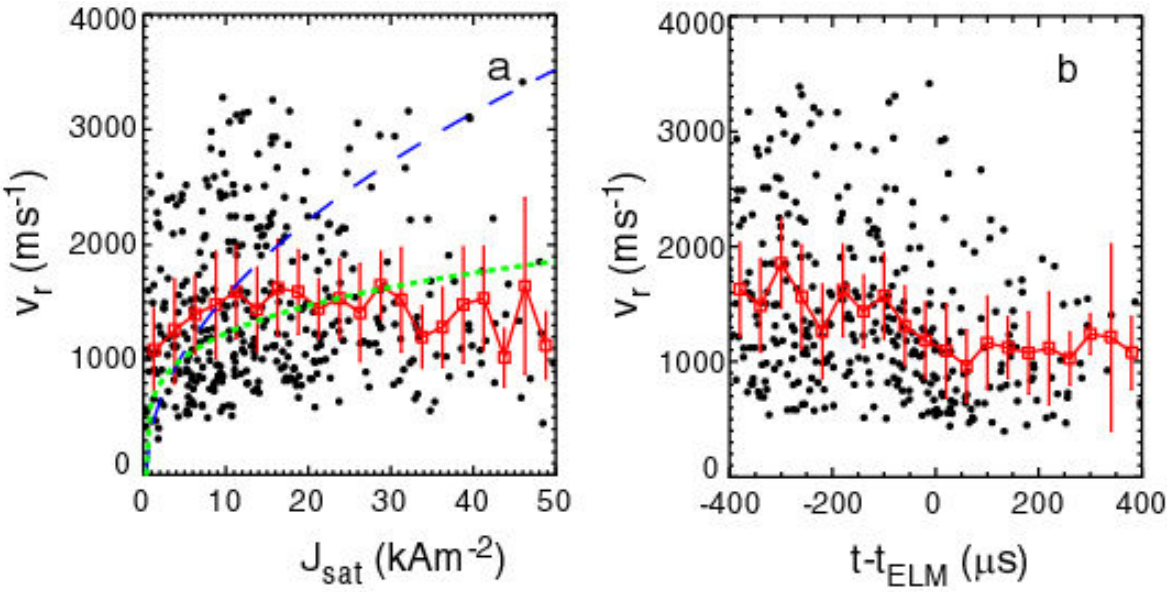

Figure 6 The radial velocity (V_r) determined from the time delay between the ion saturation current peaks from the filament probe a) as function of ion saturation current density (J_{SAT}) at the first probe and b) as a function of time relative to the peak of the diverter D_α signal (t_{ELM}). The open squares and error bars represent the binned mean and standard deviation of the distribution. The curves in a) represent a dependence of the form $V_r \propto (J_{sat})^{\alpha}$ with $\alpha = 0.25$ (dotted) and $\alpha = 0.5$ (dashed).

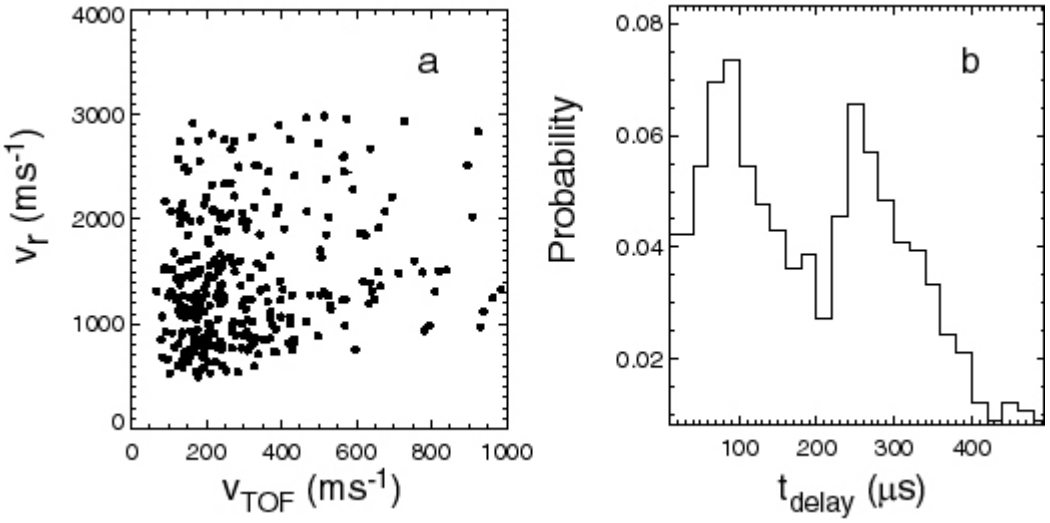

Figure 7 a) The radial velocity (V_r) determined from the time delay between the ion saturation current peaks from the filament probe versus the velocity determined form the time delay between the start of the ELM and the peak in the ion saturation current at the probe (V_{TOF}). b) The probability distribution function for the time delay between the start of the ELM and the filaments starting to move radially, assuming a constant radial velocity with distance.

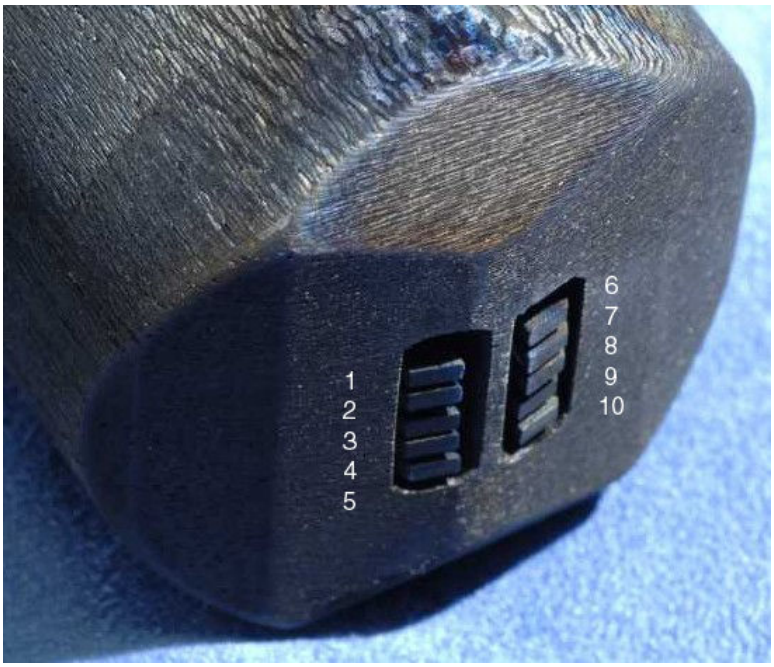

Figure 8 Probe head on reciprocating probe showing the location of the pins which can be used to measure either floating potential or ion saturation current. The pins measure 2 mm by 4.13 mm and the separation between the centre of the pins in the vertical direction is 3 mm.

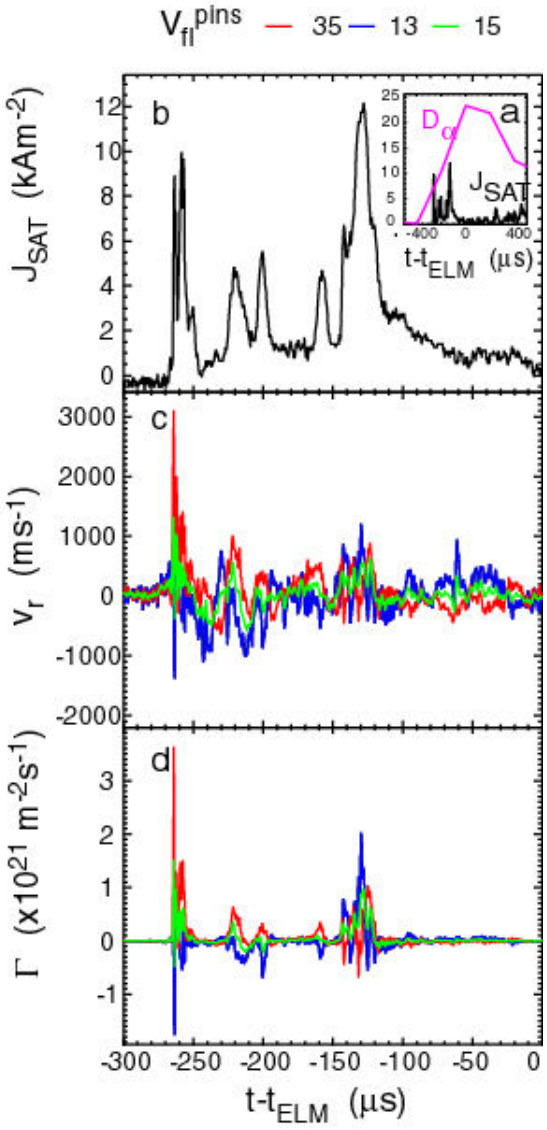

Figure 9 a) The ion saturation current (J_{SAT}) and the target D_α signal during an ELM as a function of time relative to the peak of the diverter D_α signal (t_{ELM}). b) the ion saturation current. c) the radial velocity ($E_\theta \times B/B^2$) and d) the particle flux (Γ) as function of time in the ELM calculated using the floating potential measurements from tips 3 and 5 (red curve), 1 and 3 (blue curve) and 1 and 5 (green curve).

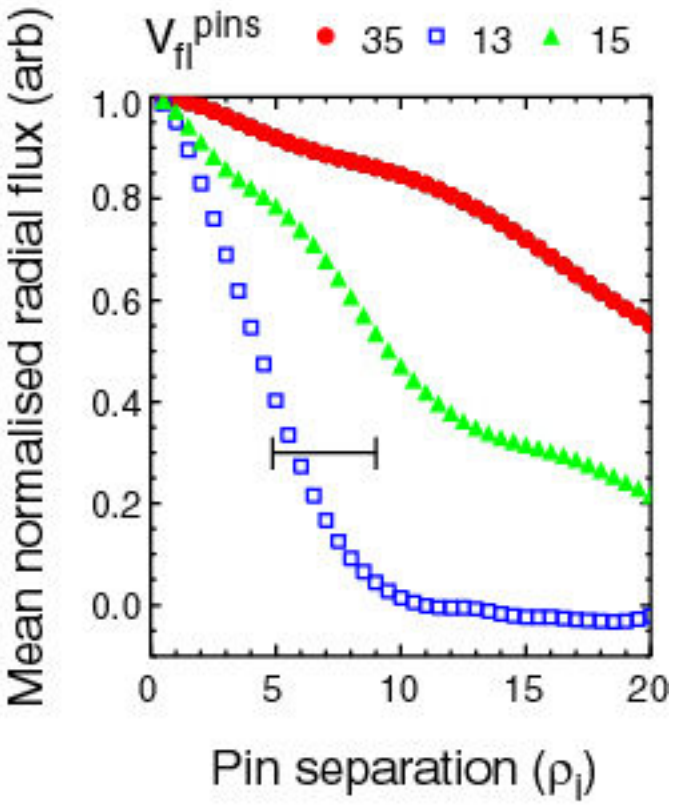

Figure 10 Calculated mean normalised radial flux as a function of pin separation obtained by using a synthetic probe diagnostic in a TOKAM-2D simulation and calculating the plasma potential and density for different probe configurations similar to that used in the experiment namely: V_{fl}^{3}-J_{SAT}^{4}-V_{fl}^{5} (circles), V_{fl}^{1}-J_{SAT}^{4}-V_{fl}^{5} (triangles) and V_{fl}^{1}-V_{fl}^{3}-J_{SAT}^{4} (squares). The horizontal line shows the range of pin separations in the experiment.

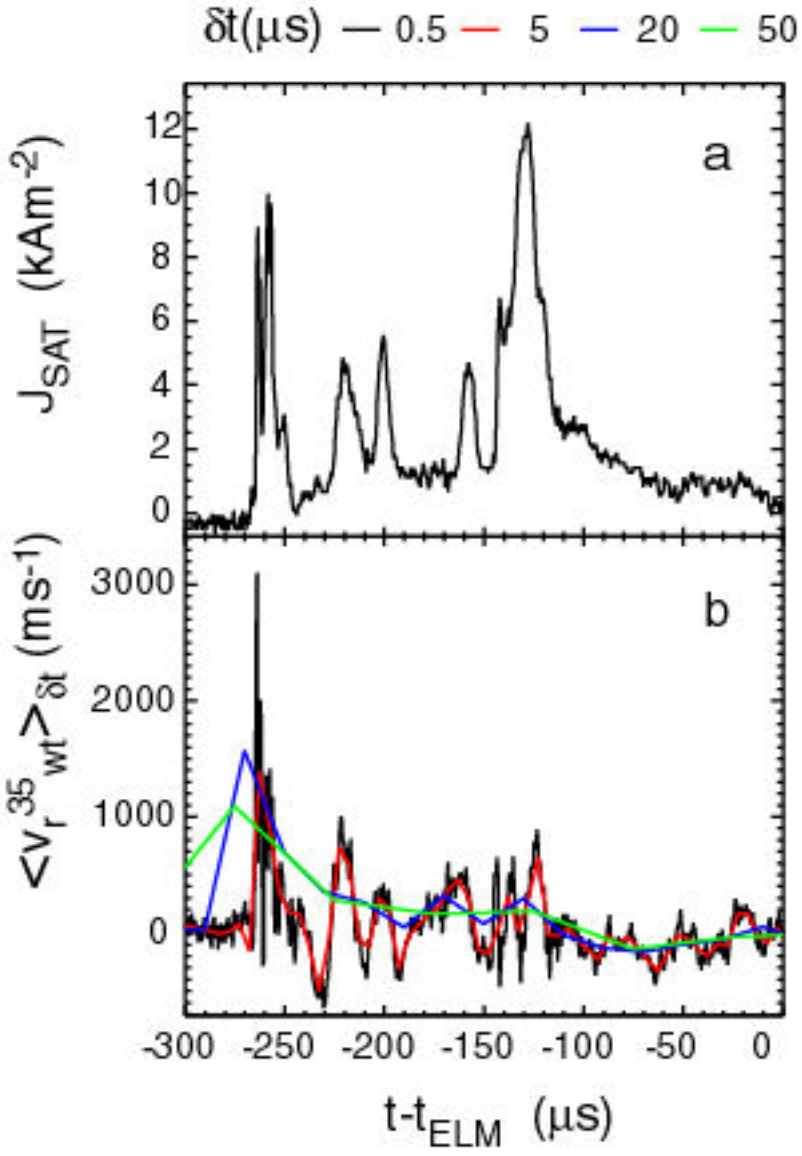

Figure 11 a) The ion saturation current as a function of time in the ELM and b) the time averaged ion saturation current weighted radial ($E_\theta \times B/B^2$) velocity using tips 3 and 5. The curves are for time averaging over 0.5 (black), 5 (red), 20 (blue) and 50 (green) μs.

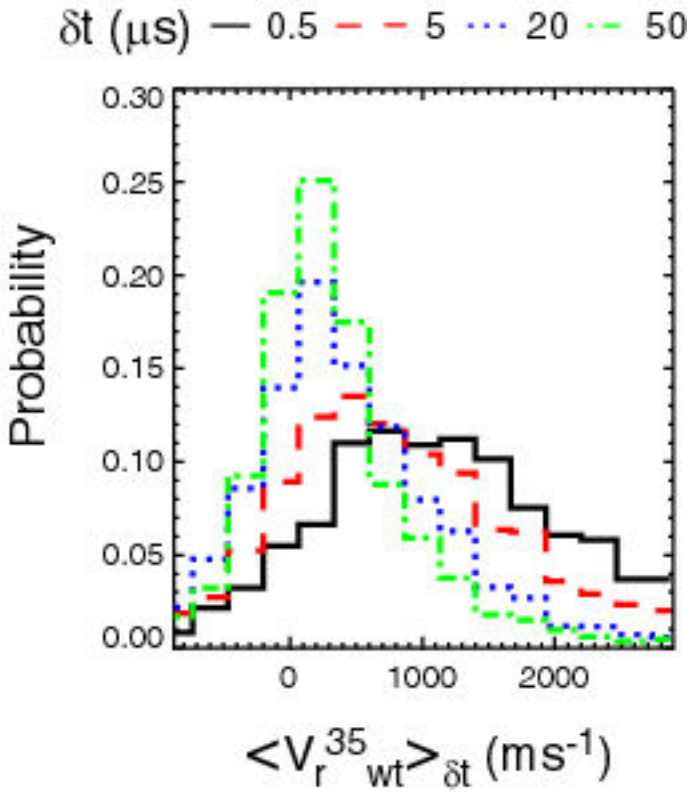

Figure 12 The probability density function of the time averaged ion saturation current weighted radial velocity ($E_\theta \times B/B^2$) using tips 3 and 5 for time averaging over 0.5 (solid), 5 (dashed), 20 (dotted) and 50 (dashed-dotted) μs.

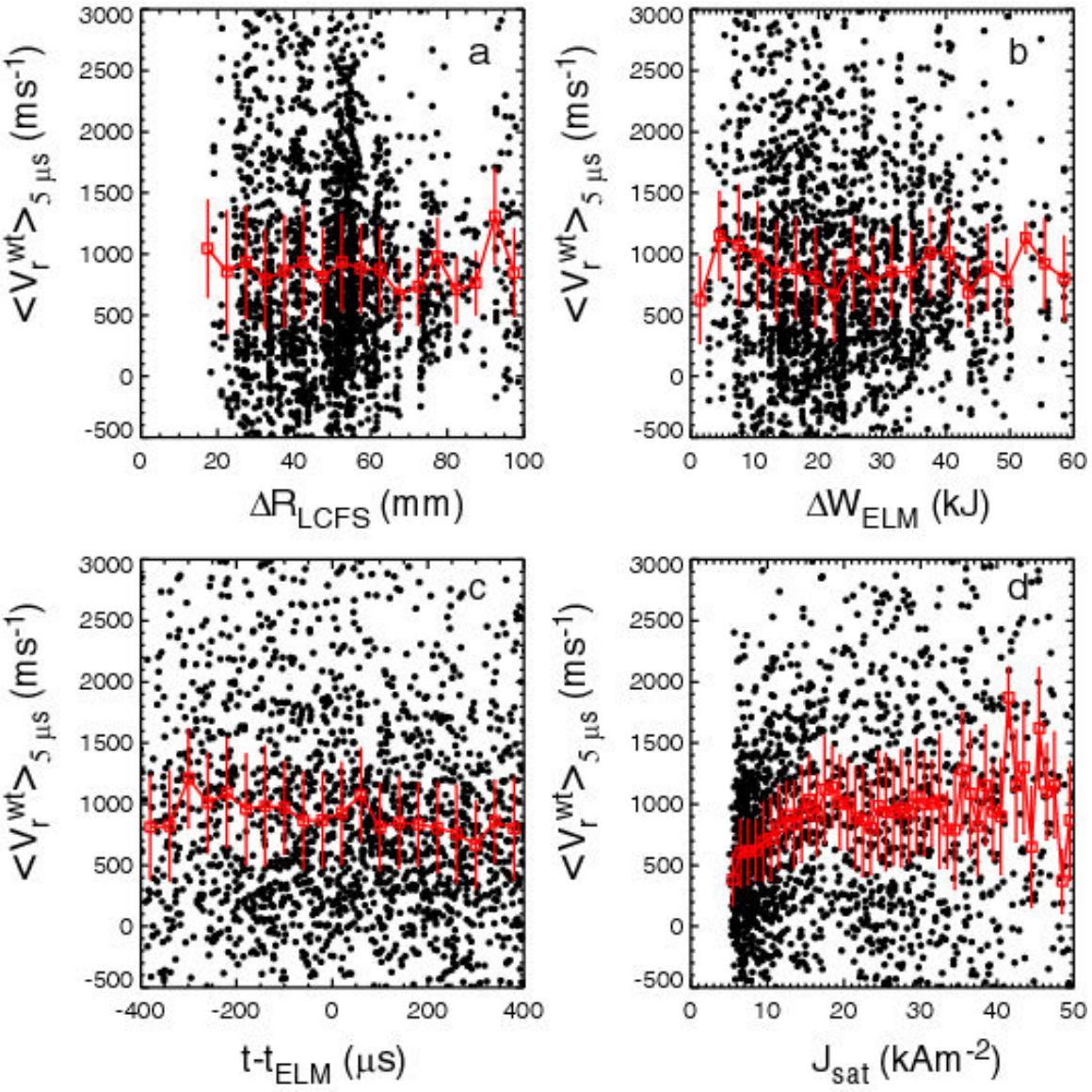

Figure 13 The time averaged ion saturation current weighted radial ($E_\theta \times B/B^2$) velocity using tips 3 and 5 for time averaging over 5 μs as a function of a) the distance from the last closed flux surface (ΔR_{LCFS}), b) ELM energy loss (ΔW_{ELM}), c) time relative to the peak of the diverter D_α signal (t_{ELM}) and d) ion saturation current density (J_{SAT}). The open squares and error bars represent the binned mean and standard deviation of the distribution.

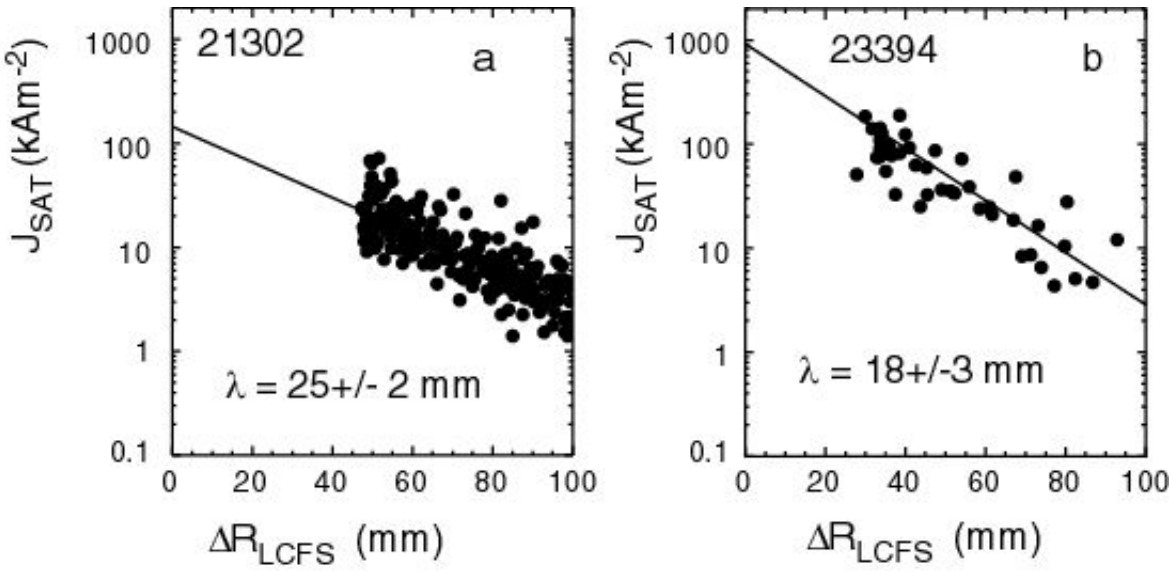

Figure 14 The peak ion saturation current of the ELM efflux observed at the mid-plane manipulator as a function of distance from the last closed flux surface (ΔR_{LCFS}) for shots with a) T_e^{ped} = 350 eV, q_{95} = 5.5 and ΔW_{ELM} = 4 kJ and b) T_e^{ped} =600 eV, q_{95} = 4.5 and ΔW_{ELM}=21 kJ. The solid curves represent the result of an exponential fit to the data to determine the e-folding length (λ).

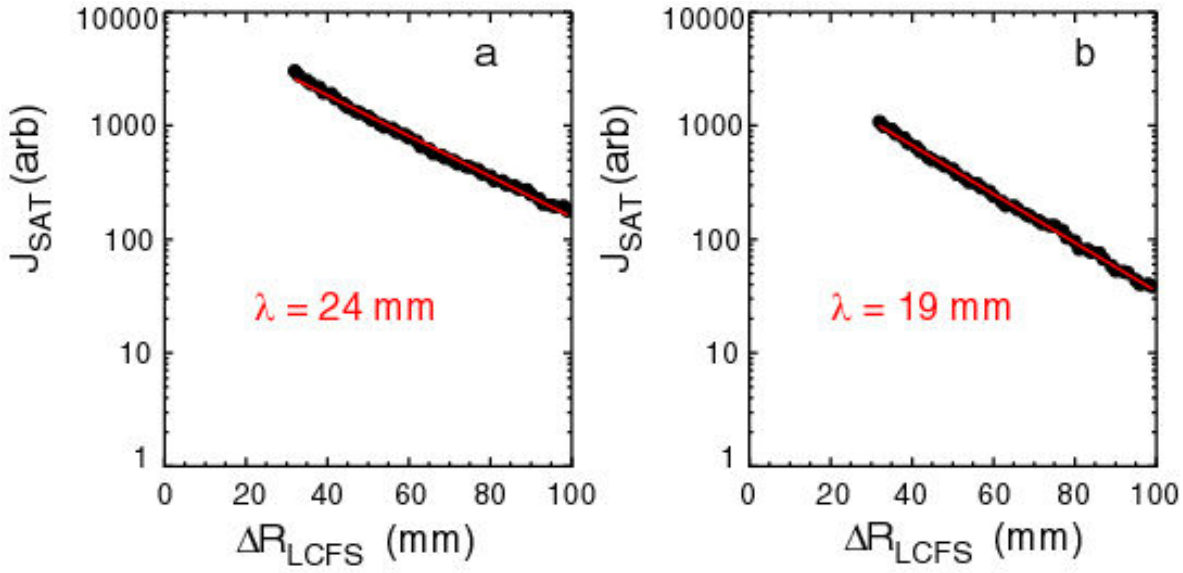

Figure 15 The radial distributions of ion saturation current at the mid-plane for simulated filaments moving with a constant radial velocity of 1.5 km s^{-1} with plasma parameters of a) T_e^{ped} = 350 eV , q_{95} = 5.5 and b) T_e^{ped} =600 eV, q_{95} = 4.5. The solid curves represent the result of an exponential fit to the data to determine the e-folding length (λ).

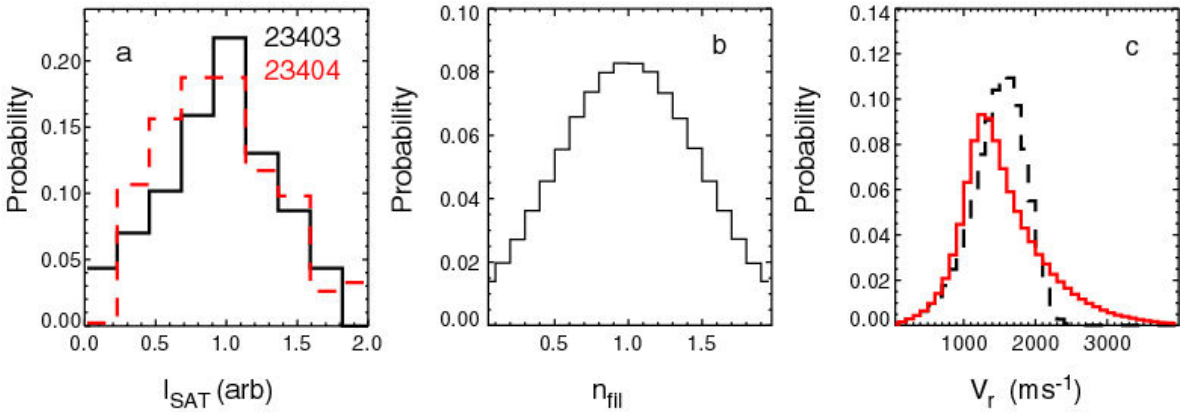

Figure 16 a) The probability distribution of the peak ion saturation current obtained during ELMs normalised to the mean obtained when the probe was at a fixed distance from the last closed flux surface for shot 23403 (solid) and 23404 (dashed). b) the probability distribution of the fraction of particles initially in each filament used in the simulations. c) The probability distribution of the velocities assuming that $V_r \propto \sqrt{n_{fil}}$ assuming perfect measurements of the time delay (dashed) and including realistic errors (solid).

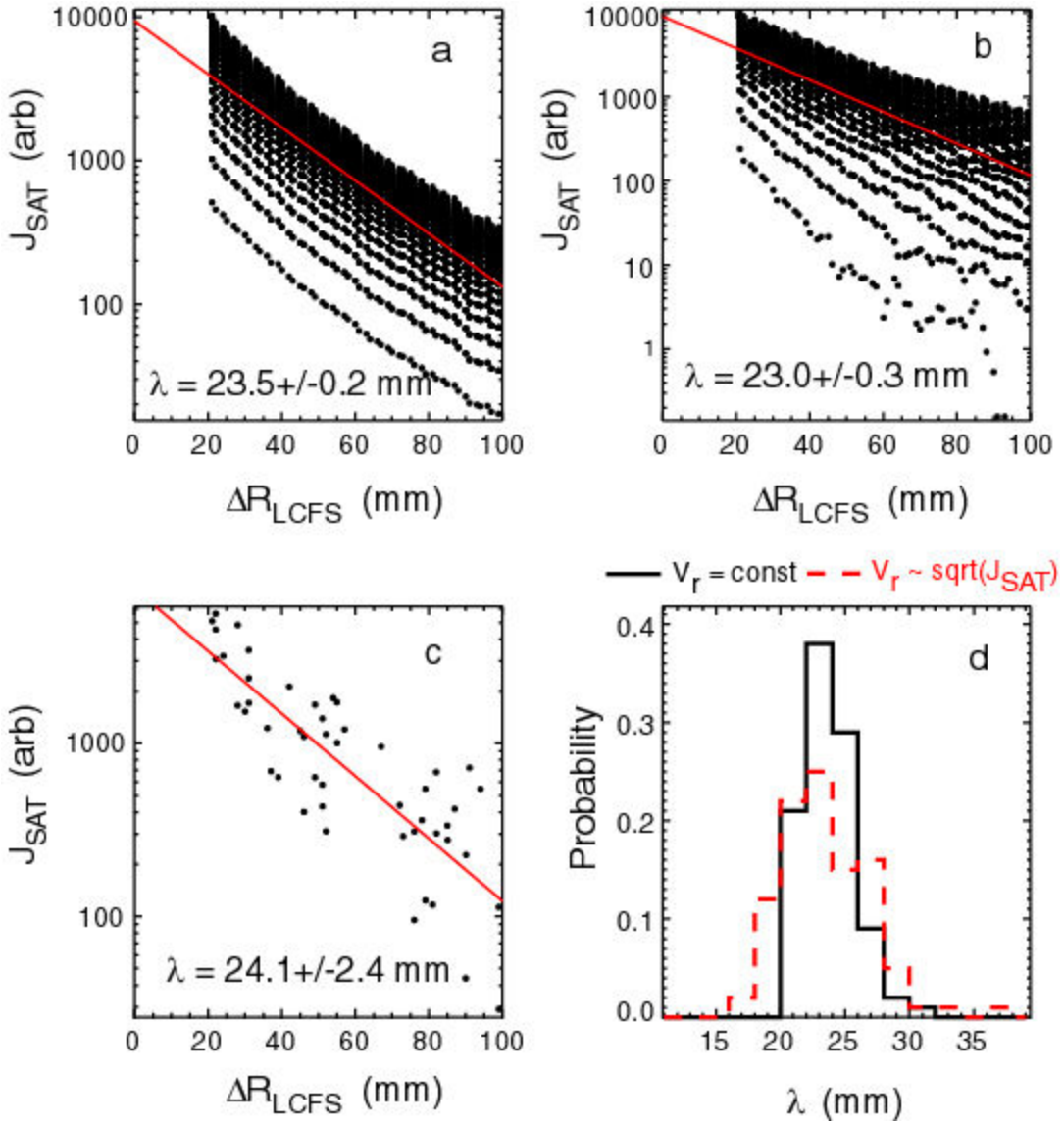

Figure 17 The radial distributions of ion saturation current at the mid-plane for simulated filaments having a range of densities moving with a) constant radial velocity of 1.5 km s^{-1} and b) assuming $V_r \propto \sqrt{n_{fil}}$. c) The radial distribution for 100 randomly selected events from the distribution in b). The solid curves represent the result of an exponential fit to the data to determine the e-folding length (λ). d) The probability distribution of the e-folding length measured by fitting 100 randomly selected distributions assuming constant velocity (solid) and $V_r \propto \sqrt{n_{fil}}$ (dashed).

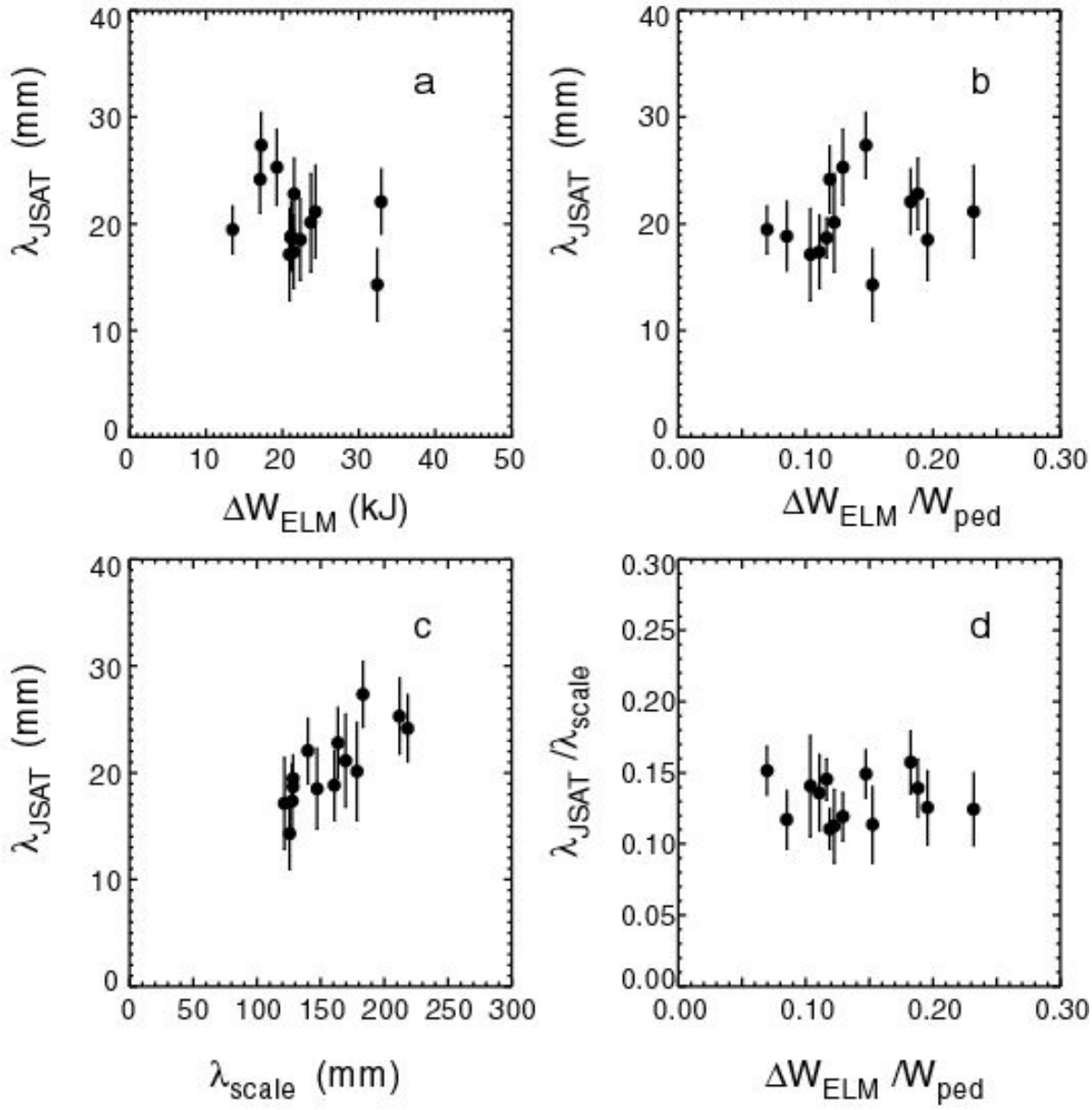

Figure 18 The ion saturation current e-folding length (λ_{JSAT}) as a function of a) ELM energy loss (ΔW_{ELM}), b) ELM energy loss normalised to the pedestal energy ($\Delta W_{ELM}/W_{PED}$) and c) an e-folding length scaling ($\lambda_{scale} = V_r L_{//}/c$). d) λ_{JSAT} normalised by λ_{scale} as a function of ELM energy loss normalised to the pedestal energy.